A model of the entrance pupil of the human eye

Geoffrey K Aguirre[1,*]

[1]Department of Neurology, Perelman School of Medicine, University of Pennsylvania, Philadelphia, PA 19104, USA
[*]aguirreg@upenn.edu

ABSTRACT

The pupil aperture of the iris is subject to refraction by the cornea, and thus an outside observer sees a virtual image: the "entrance pupil" of the eye. When viewed off-axis, the entrance pupil has an elliptical form. The precise appearance of the entrance pupil is the consequence of the anatomical and optical properties of the eye, and the relative positions of the eye and the observer. This paper presents a ray-traced, exact model eye that provides the parameters of the entrance pupil ellipse for an observer at an arbitrary location. The model is able to reproduce empirical measurements of the shape of the entrance pupil with good accuracy. I demonstrate that accurate specification of the entrance pupil of a stationary eye requires modeling of corneal refraction, the misalignment of the visual and optical axes, and the non-circularity of the pupil aperture. The model, including a three-dimensional ray-tracing function through quadric surfaces, is implemented in open-source MATLAB code.

Introduction

The pupil is the aperture stop of the optical system of the eye. When viewed from the outside, an observer sees the entrance pupil of the eye, which is the image of the pupil as seen through corneal refraction. The precise appearance of the entrance pupil depends upon the anatomical and optical properties of the eye, as well as the relative positions of the eye and the observer. Characterization of the entrance pupil is relevant for modeling the off-axis image-forming properties of the eye (1), optimizing corneal surgery (2), and performing model-based eye-tracking (3).

The appearance of the entrance pupil as a function of horizontal viewing angle has been the subject of empirical measurement over some decades (4; 5). As an observer views the eye from an increasingly oblique angle, the pupil takes on an ever-more ellipitical appearance. Mathur and colleagues (6) measured the shape of the entrance pupil as a function of the nasal and temporal visual field position of a camera moved about a stationary eye. The ratio of the minor to major axis length of the pupil ellipse (essentially the horizontal-to-vertical aspect ratio) was well fit by a decentered and flattened cosine function of viewing angle. Fedtke and colleagues (7), using optical bench software, obtained a function with similar form by ray trace simulation of a spherical cornea(8). As will be developed, the fit of this previous model to empirical data is imperfect.

Here I present a ray-traced model eye that provides the ellipse parameters of the entrance pupil as seen by an observer at an arbitrary location. The model accounts for individual variation in biometric parameters, including spherical refractive error. The location of the fovea is specified and used to derive separate visual and optical axes. The open-source MATLAB code (`https://github.com/gkaguirrelab/gkaModelEye`) implements an invertible ray-tracing solution that can incorporate artificial lenses (e.g., spectacles, contacts) in the optical path between eye and observer. I simulate the circumstances of the Mathur and colleagues study (6) and show that their measurements can be replicated with good accuracy if the model incorporates *i*) corneal refraction, *ii*) the separation of the visual and optical axes, and *iii*) the non-circularity and tilt of the aperture stop.

Model eye

In this section I describe the properties of a model eye specified in software. The parameters of the model are derived from prior reports (principally (9; 10)), with some modifications. Several aspects of the model vary with the spherical equivalent error of the eye. The coordinate system is centered on the optical axis, with the dimensions corresponding to axial, horizontal, and vertical position. Units are given in mm and degrees, with the exception of the tilt component of the ellipse parameters, which is specified in radians. Axial depth is given relative to the anterior-most point of the front surface of the cornea, which is assigned a depth position of zero. Parameters are presented for a right eye. Horizontal and vertical schematic sections of the model eye are presented in Figure 1.

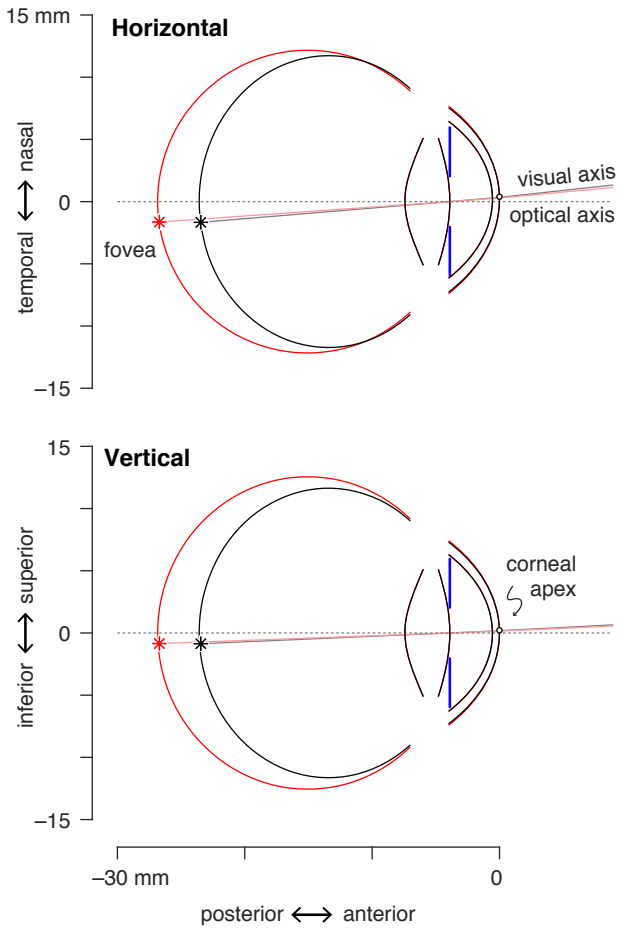

Figure 1. Schematic of the model eye The components of the model are shown for two right eyes with differing spherical refractive errors. In black is the model of an emmetropic eye, and in red that of an eye with a –10 refractive error. The myopic eye has a larger, and more spherical, vitreous chamber. The model specifies the location of the fovea (asterisk); myopia brings the fovea closer to the posterior apex of the vitreous chamber. Consequently the visual axis (solid line) moves to closer alignment with the optical axis (dotted line). A subtle difference in the curvature of the front corneal surface between the emmetropic and myopic eyes may be seen.

Anatomical components

Cornea

The front surface of the cornea is modeled as a tri-axial ellipsoid, taking the "canonical representation" from (9) for the emmetropic eye. Atchison and colleagues (10) observed that the radius of curvature at the vertex of the cornea varies as a function of spherical ametropia, and provided the parameters for a rotationally-symmetric, prolate ellipsoid, with the radius of curvature (but not asphericity) varying linearly with the refractive error of the modeled eye. I calculated the proportional change in the Navarro values that would correspond to the effect modeled by (10). This yields the following expression for the radii of the corneal front surface ellipsoid:

$$cornea_front_radii(SR) = \begin{bmatrix} 14.26 & 10.43 & 10.27 \end{bmatrix} \cdot (1 - 0.0028SR) \tag{1}$$

where SR is spherical refractive error in diopters, and the radii are given in the order of $\begin{bmatrix} axial & horizontal & vertical \end{bmatrix}$.

Atchison and colleagues (10) found that the back surface of the cornea did not vary by ametropia. Navarro and colleagues (9) did not provide posterior cornea parameters. Therefore, I scale the parameters provided by Atchison (10) to be proportional to the axial corneal radius specified by Navarro:

$$cornea_back_radii = \begin{bmatrix} 13.7716 & 9.3027 & 9.3027 \end{bmatrix} \tag{2}$$

The center of the back cornea ellipsoid is positioned so that there is 0.55 mm of corneal thickness between the front and back surface of the cornea at the apex, following (10).

Navarro and colleagues (9) measured the angle of rotation of the axes of the corneal ellipsoid relative to the keratometric axis (the axis that connects a fixation point with the center of curvature of the cornea). I converted these angles to be relative to the optic axis of the eye, yielding the parameters –3.45, 1.44, and –0.02, degrees azimuth, elevation, and torsion. These describe a corneal ellipsoid that is tilted (relative to the optical axis) so that the corneal apex is directed towards the superior, nasal field.

Iris and pupil

The iris is modeled as a plane perpendicular to the optical axis (i.e., zero "iris angle"), with the anterior surface positioned at a depth equal to the anterior point of the lens. The anterior surface of the iris is positioned 3.9 mm posterior to the anterior surface of the cornea for the cycloplegic eye (11).

The pupil is an aperture in the iris, centered on the optical axis. The pupil aperture is modeled as slightly non-circular. Wyatt (12) measured the average (across subject) ellipse parameters for the entrance pupil under dim and bright light conditions (with the visual axis of the eye aligned with camera axis). The pupil was found to be elliptical in both circumstances, with a horizontal long axis in bright light, and a vertical long axis in dim light. The elliptical eccentricity was less for the constricted as compared to the dilated pupil (non-linear eccentricity ε = 0.12 horizontal; 0.21 vertical; where the ratio of the minor to the major axis of an ellipse is equal to $\sqrt{1-\varepsilon^2}$). In the current model, I limit the eccentricity of the dilated entrance pupil to a slightly lower value (0.17) to provide a better fit to the measurements of Mathur and colleagues (6) (discussed below). Accounting for the refraction of the cornea (using ray-tracing simulations), I calculated the ellipse parameters (area, eccentricity, and tilt) for the pupil aperture that would produce the entrance pupil appearance observed by Wyatt (12) at the two light levels. A hyperbolic tangent function of pupil aperture radius is then used to transition between the elliptical eccentricity of the constricted pupil—through circular at an intermediate size—to the eccentricity of the dilated pupil. Consistent with Wyatt (12), the tilt of the elliptical pupil aperture is horizontal (θ = 0) for all pupil sizes below the circular intermediate point, and then vertical with a slight tilt of the top towards the nasal field for all larger pupils.

The model therefore provides a pupil that smoothly transitions in elliptical eccentricity and horizontal-to-vertical orientation (passing through circular) as the radius of the pupil aperture varies from small to large following these functions:

$$\begin{aligned} \varepsilon(r) &= 0.145(4.770(tanh(r-1.749)+0.099)) \\ \theta(\varepsilon) &= \begin{cases} 0 & \text{if } \varepsilon < 0; \\ \frac{3}{7}pi & \text{if } \varepsilon > 0; \end{cases} \end{aligned} \tag{3}$$

where r is the radius of the pupil aperture in mm, ε is the non-linear eccentricity of the aperture ellipse, and θ is the tilt of the aperture ellipse (horizontal = 0; vertical = $pi/2$). The sign of ε is used to determine θ, although the absolute value of ε is used to generate the pupil aperture ellipse.

Although not required to determine the entrance pupil, the boundary of the visible iris is modeled for comparison with empirical images of the eye. The horizontal visible iris diamter (HVID) has been reported to be 11.8 mm (13). Bernd Bruckner

of the company Appenzeller Kontaktlinsen AG measured HVID using photokeratoscopy in 461 people (14) and kindly supplied me with the individual subject measurements. These data are well fit with a Gaussian distribution and yield a mean iris radius of 5.91 mm and a standard deviation of 0.28 mm. After accounting for corneal magnification, the radius of the iris in the model is set to 5.57 mm.

Lens

The crystalline lens is modeled as a set of quadric surfaces. The anterior and posterior surfaces of the lens are modeled as one-half of a two-sheeted hyperboloid. The radii of these surfaces, their dependence upon age and the accommodative state of the eye, and thickness of the anterior and posterior portions of the lens, are taken from Navarro and colleagues (15). The interior of the lens is modeled with a gradient of refractive indices. This is realized as a set of ellipsoidal iso-indicial surfaces; 40 surfaces were used in the results presented here. The particular parameters are taken from Atchison (10), which were in turn derived from prior studies (16; 17). The lens is modeled as center-aligned with the optical axis. The axial position of the lens center is taken from Atchison (10).

Vitreous chamber and retina surface

Atchison (10) provides the radii of curvature and asphericities of a biconic model of the vitreous chamber, which is decentred and tilted with respect to the visual axis. With increasing negative refractive error (myopia), the vitreous chamber changes size, elongating in the axial direction and to a lesser extent in the vertical and horizontal directions. I model the vitreous chamber as an ellipsoid that is centered on and aligned with the optical axis, taking the radii, and their dependence upon spherical refractive error, from equations 22-24 provided by (10).

Visual axis

Our goal is to describe the appearance of the entrance pupil. Often, the pupil is observed while the subject under study has their eye directed at a fixation point. To model this, I specify the visual axis of the eye, and its angle with respect to the optical axis. The visual axis is defined by the ray that connects the fovea of the eye with the fixation target. The angle between the visual and optical axes of the eye is termed α.[1].

The visual axis is generally displaced nasally and superiorly within the visual field relative to the optical axis. The horizontal displacement of the visual axis is $5-6^\circ$ (19); vertical displacement is on the order of $2-3^\circ$ (20; 21; 22).

Angle α is known to vary by spherical refractive error (19**?**), becoming smaller in myopia. The precise relationship between α and spherical refractive error is poorly defined, principally due to the limited number of measurements that have been made for cases of extreme myopia. In the current model, I adopt the theoretically motivated relationship presented by Tabernero and colleagues (19) (after converting the referent of their expression from axial length to spherical error, using the relationship given by Atchison (10), eq. 19):

$$\alpha(SR) = tan^{-1}\left[\left(\frac{16.5}{16.5-0.299SR}\right)tan(\alpha_0)\right] \tag{4}$$

where α_0 is the angle of the visual axis with respect to the optical axis in the emmetropic eye, and SR is spherical refractive error in diopters. I set the $\alpha_0 = 5.8^\circ$ in the horizontal direction and $\alpha_0 = 3^\circ$ in the vertical direction. Ray tracing through the model eye is used to identify the foveal point on the retinal surface for which a ray that passes through the optical system of the eye exits the cornea at the α angles.

Perspective projection and ray-tracing

Given the model eye, I then specify the appearance of the pupil in an image in terms of the parameters of an ellipse. This is accomplished by perspective projection of the eye to the sensor of a simulated camera, and then fitting an ellipse to points on the border of the pupil image. This projection requires us to specify the intrinsic properties of a camera and its position in space.

Perspective projection

A pinhole camera model is defined by an intrinsic matrix. This may be empirically measured for a particular camera using a resectioning approach (23; 24).[2] If provided, the projection will also model radial lens distortion (25), although the simulations performed here assume no radial distortion. The position of the camera relative to the eye is specified by a translation vector in world units, and the rotation of the camera about its optical axis (torsion).

With these elements in place, the model defines equally spaced points on the boundary of the pupil aperture with a specified radius in millimeters. As the pupil aperture is elliptical, radius is defined in terms of a circle of equivalent area. Five boundary

[1] I adopt the axis terms and Greek letter designations of Atchison and Smith (18). The related value of κ is the angle between the visual and pupillary axes. In this section I cite studies that have measured variation in both of these angles, but for simplicity refer to only α in the text.

[2] This is also termed "camera calibration" but the term "resectioning" is preferred here as it avoids confusion with spectroradiometric calibration of a device.

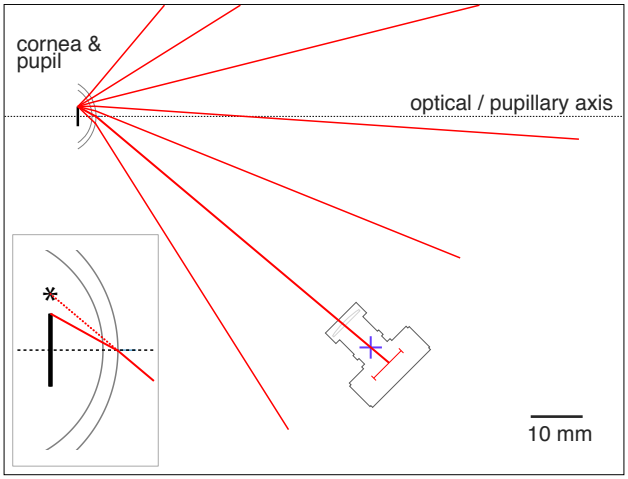

Figure 2. Calculation of the virtual image location of a pupil boundary point This 2D schematic shows the cornea and a 2 mm radius pupil aperture of the model eye. A camera is positioned at a 45° viewing angle relative to the optical axis of the eye. The optical system is composed of the aqueous humor, the back and front surfaces of the cornea, and the air. We consider the set of rays that might originate from the edge of the pupil. Each of these rays depart from the pupil aperture at some angle with respect to the optical axis of the eye. We can trace these rays through the optical system. Each ray will pass at a varying distance from the pinhole aperture of the camera (blue +). For a pinhole camera, only the ray that strikes the aperture point exactly (i.e., at a distance of zero) will contribute to the image. We therefore search across values of initial angle to find the ray that minimizes the intersection point distance. In this example system, a ray that departs the pupil point at an angle of $-30°$ with respect to the optical axis of the eye strikes the aperture of the camera after undergoing refraction by the cornea. *Inset bottom left*. Given the path of the ray after it exits the last surface of the optical system (in this case, the front surface of the cornea), we can project back to the plane of the pupil, and assign this as the point in the coordinate space from which the ray appeared to originate. This is the virtual image location for this pupil point.

points uniquely specify an ellipse; six or more are required to measure the deviation of the shape of the pupil boundary from an elliptical form. The boundary points are projected to the image plane and then fit with an ellipse (26), yielding the ellipse parameters.

Ray tracing

As viewed by the camera, the pupil boundary points are subject to corneal refraction, and thus are virtual images. The cornea causes the imaged pupil to appear larger than its actual size, and displaces and distorts the shape of the pupil when the eye is viewed off-axis (3; 7). A similar and additional effect is introduced if the eye is observed through corrective lenses worn by the subject (e.g., contacts or spectacles).

To account for these effects, the projection incorporates a ray-tracing solution. I model the cornea of the eye and any corrective lenses as quadric surfaces. The set of surfaces (with their radii, rotations, translations, and refractive indices) constitute the optical system. The routines provide refractive indices for the aqueous humor and cornea, as well as values for materials that are present in the optical path as artificial corrective lenses (e.g., hydrogel, polycarbonate, CR-39). The refractive indices specified by the model account for the spectral domain in which the eye appearance is being modeled (i.e., visible or near infrared), with the specific values derived from a variety of sources (27; 28; 29; 30; 31). The position, curvature, and thickness of any modeled corrective lenses are computed by the analysis routines, based upon the specified spherical correction of the lens in diopters.

For the specified optical system, I implement 3D tracing for skew rays through a system of quadric surfaces (32). Given a boundary point on the pupil aperture, the angles with which the ray departs from the optical axis of the eye, and the spatial translation of the camera, we can compute how closely the ray passes the pinhole aperture of the camera (Figure 2). We search for the ray that exactly intersects the camera aperture and thus will uniquely be present in the resulting image (assuming a pinhole aperture). Given the position and angle of this ray as it leaves the last surface in the optical system, we can project back to the apparent (virtual) point of origin of the ray in the pupil plane.

Entrance pupil of a stationary eye

The ellipse parameters of the entrance pupil produced by the current model may be compared to empirical measurements. Mathur and colleagues (6) obtained images of the pupil of the right eye from 30 subjects. Each subject fixated a target. A camera was positioned 100 mm away from the corneal apex and was moved to viewing angle positions in the temporal and

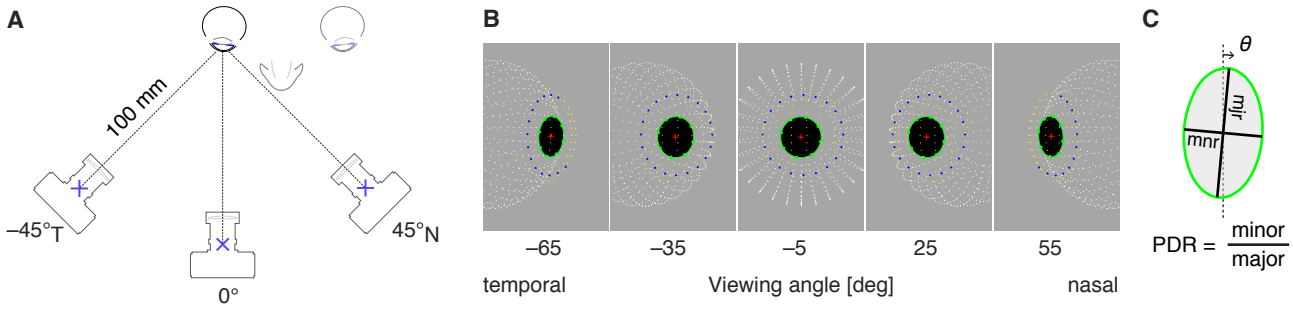

Figure 3. Simulation of measurements of Mathur and colleagues 2013. (A) A camera was positioned 100 mm from the cornea at different viewing angles within the temporal and nasal visual field. The visual axis of the eye was aligned with the optical axis of the camera at a viewing angle of zero. (B) The output of the current model is shown for equally spaced (30°) viewing angles from the temporal to nasal visual field. In the center image, viewed at –5°, the optical axes of the eye and camera are nearly aligned in the horizontal plane. The points shown correspond to the vitreous chamber (white), visible iris border (blue), pupil border points and fitted ellipse (green), front corneal surface (yellow), and the center of the pupil aperture (red plus). The iris border and pupil border points have been subjected to refraction by the cornea. Iris border points are missing in some views as these points encountered total internal reflection during ray tracing. (C) The pupil diameter ratio (PDR) is the ratio of the minor to the major axis of an ellipse fit to the entrance pupil. θ is the tilt of the major axis of the pupil ellipse.

nasal visual field within the horizontal plane. A viewing angle of zero was assigned to the position at which the visual axis of the subject was aligned with the optical axis of the camera. At each angular viewing position, the camera was translated slightly to be centered on the entrance pupil. The pupil of the subject was pharmacologically dilated (and the eye rendered cycloplegic) with 1% cyclopentolate. The subjects had a range of spherical refractive errors, but the central tendency of the population was to slight myopia; I calculated the weighted mean spherical error to be –0.823 diopters. Figure 3a illustrates the geometry of the measurement.

The measurements of Mathur and colleagues (6) can be simulated in the current model. I created a right eye with a spherical refractive error of –0.823 diopters, and assumed an entrance pupil diameter of 6 mm to account for the effect of cyclopentolate dilation (33) (accounting for corneal magnification, this corresponds to a 5.3 mm diameter pupil aperture). I rotated the eye so that the visual axis was aligned with the optical axis of the camera at a visual field position of zero. I then positioned the camera as described in (6). Figure 3b presents renderings of the model eye as viewed from the nasal and temporal visual field.

Pupil diameter ratio

At each viewing angle Mathur and colleagues (6) measured the ratio of the minor to the major axis of the entrance pupil, termed the pupil diameter ratio (PDR; Figure 3c). These measurements were combined across subjects and accurately fit by a parameterized cosine function. Figure 4a shows the resulting fit to the empirical data. The PDR decreases as a function of viewing angle, as the entrance pupil is tilted away from the camera and the horizontal axis is foreshortened. The observed entrance pupil follows a cosine function that is "both decentered by a few degrees and flatter by about 12% than the cosine of the viewing angle."(6)

Using the current model, I calculated the PDR for the entrance pupil with the camera positioned at a range of viewing angles. The model output (Figure 4b; red dashed line) agrees well with the empirical measurements. In prior work, Fedtke and colleagues (7) examined the properties of a simulated entrance pupil, assuming a rotationally symmetric cornea, a circular pupil aperture, and in which the visual and optical axes were aligned. The PDR of their model as a function of viewing angle is plotted in blue in Figure 4c.

We may examine how components of the current model contribute to the replication of the empirical result. The simulation was repeated with successive addition of model components. The simplest model assumes a circular pupil aperture, no corneal refraction, and alignment of the optical and visual axes of the eye. Under these circumstances the entrance pupil behaves exactly as a function of the cosine of the viewing angle (Figure 5a). Next, we rotate the eye so that the visual axis is aligned with the optical axis of the camera when the viewing angle is zero (Figure 5b). Modeling of α (the misalignment of the visual and optical axes) decenters the PDR function. Addition of refraction by the cornea (Figure 5c) flattens the PDR function, as the entrance pupil now demonstrates magnification along the horizontal axis with greater viewing angles. Finally, the model is augmented with an elliptical pupil aperture (Figure 5d). Because the dilated pupil aperture is itself taller than it is wide, the PDR function is reduced overall, bringing the model into final alignment with the empirical result.

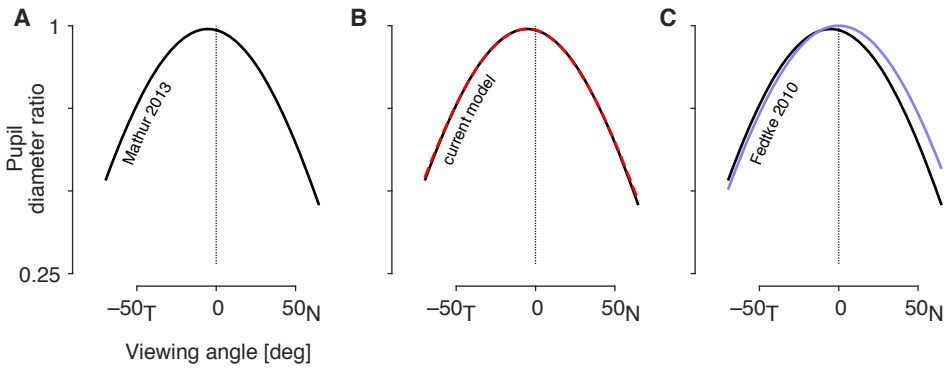

Figure 4. Empirical and modeled pupil diameter ratios. (a) The PDR as a function of viewing angle that was observed by Mathur and colleagues in 30 subjects. Note that the peak PDR is slightly less than one, indicating that the pupil always had an elliptical shape with a vertical major axis in these measurements. Also, the peak value is shifted away from a viewing angle of zero. (b) The current model provides the parameters of the entrance pupil ellipse. When the experimental conditions of Mathur and colleagues are simulated in the model, the resulting PDR function (dashed red line) agrees well with the empirical result (black). (c) In blue is the output of a model of the entrance pupil presented by Fedtke and colleagues in 2010.

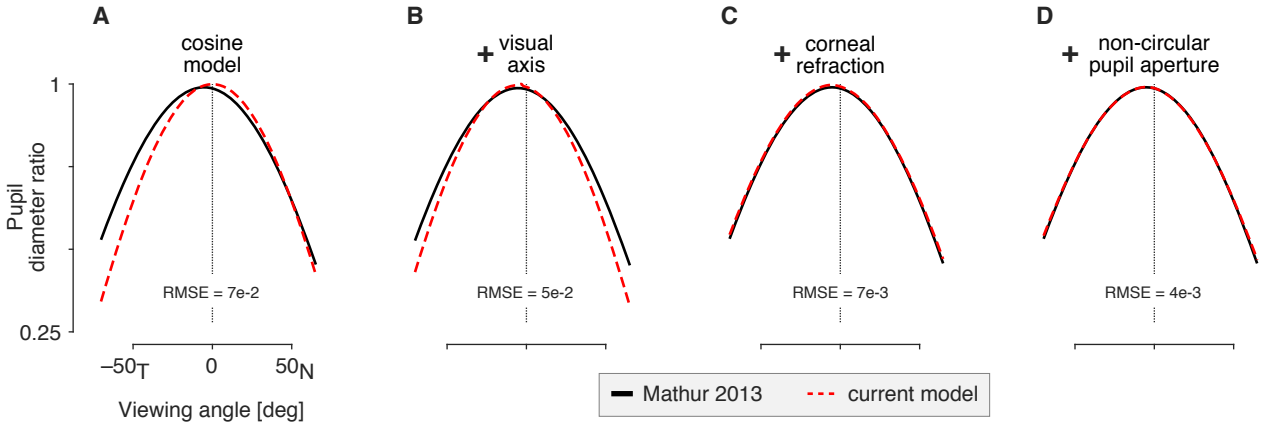

Figure 5. Effect of model components upon the entrance pupil diameter ratio function. In black is the Mathur and colleagues (2013) empirical result. The dashed red line is the behavior of the current model with the successive addition of model components (a-d). The root mean squared error (RMSE) between the model and the Mathur empirical result is given in each panel.

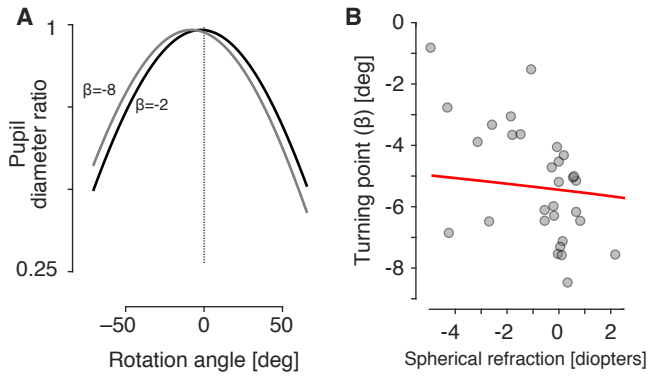

Figure 6. Variation in turning point. (A) The pupil diameter ratio was calculated using Equation 5 using $D = 0.98$, $E = 1.14$, and β values of -8 and -2. (B) In each of 30 subjects, Mathur and colleagues (2013) measured the viewing angle at which the peak pupil diameter ratio was observed (β), and related that value to the spherical refractive error of the subject. These data points (gray) are shown, along with turning point values returned by the current model when supplied with an eye of varying refractive error (red line).

Variation in the pupil diameter ratio function

Mathur and colleagues (6) found that the empirical PDR function could be fit with great accuracy by the expression:

$$PDR(\phi) = Dcos\left[\frac{\phi - \beta}{E}\right] \tag{5}$$

where ϕ is the viewing angle in degrees, D is the peak PDR, β is the viewing angle at which the peak PDR is observed (e.g., the "turning point" of the function), and $180E$ is the half-period of the fit in degrees. When fit to the output of the current model, we recover the parameters $D = 0.99$, $\beta = -5.32$, and $E = 1.13$, which are quite close to the parameters found by (6) (0.99, –5.30, and 1.12) in the fit to empirical data.

We may consider how biometric variation in the model changes the observed entrance pupil in terms of these parameters. The value D reflects almost entirely the eccentricity and tilt of the pupil aperture ellipse (Eq. 3), with an additional, small effect of the vertical component of α. Wyatt (12) found individual variation in pupil shape. While this variation in pupil aperture ellipticity will produce variations in D, overall this model component had a rather small effect upon the simulated PDR (Figure 5).

The value β is determined by the horizontal component of the misalignment of the visual and optical axes of the eye (α), which can vary substantially by subject and is related to spherical refractive error. Figure 6A illustrates the PDR function associated with two different β values. Mathur and colleagues (6) obtained β for each of their 30 subjects and related this to subject variation in spherical refractive error. Figure 6B replots their data (gray points). In the current model, the value assigned to α based upon spherical refractive error is made to follow the relationship proposed by Tanernero and colleagues (19), producing the resulting behavior of the current model (red line).

The value E varies the "width" of the PDR function (Figure 7A). In their simulation, Fedtke and collagues (7) found that increasing the modeled pupil aperture slightly widened the PDR function (i.e., the parameter E increased). I examined the behavior of the current model with changes in biometric components (Figure 7B). Changes in pupil diameter had a small effect upon the shape of the entrance pupil, as described by Fedtke an colleagues. Changes in the depth of the iris relative to the corneal surface had a minimal effect, suggesting that changes in accommodation (apart from a change in pupil size) will have little effect upon the shape of the entrance pupil. I examined as well the effect of the angle with which the camera is moved across viewing position, from horizontal to oblique to vertical (Figure 7C). Because the cornea is astigmatic, an observer that moves across horizontal viewing angles encounters a different profile of corneal curvature than does an observer moving across vertical viewing angles. The current model returns an E value of 1.13 for variation in horizontal viewing angle, and a value of 0.9 across vertical viewing angle. This finding indicates that the precise values of corneal curvature and the azimuth and elevation with which the eye is observed has a meaningful effect upon the appearance of the entrance pupil.

Tilt of the entrance pupil ellipse

Mathur and colleagues (6) measured the "oblique component of pupil ellipticity" (termed component "C"), which reflects the tilt of the major axis of the pupil ellipse away from vertical. I calculated this component for the current model and found that the result compares quite well with the empirical measurements (Figure 8). This tilt component of the entrance pupil ellipse can

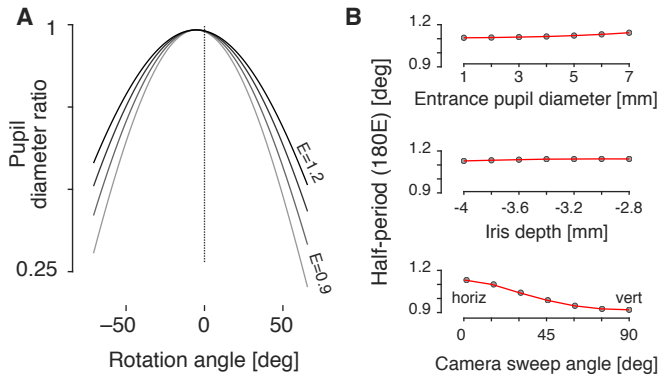

Figure 7. Variation in half-period width. (A) The pupil diameter ratio was calculated using Equation 5 using $D = 0.98$, $\beta = -5.30$, and E values ranging from 0.9 to 1.2. (B) The simulation was conducted with variation in pupil size, (*top*) iris depth (*middle*), and (*bottom*) the torsional angle with which the camera was swept across viewing position. Variation in the E parameter assessed. Cubic-spline fits to the points are shown in red.

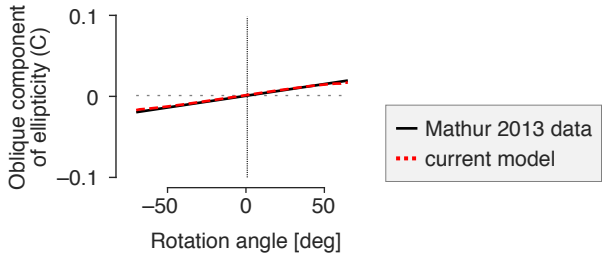

Figure 8. Oblique component of pupil ellipticity. The tilt of the pupil ellipse varies with viewing angle. Mathur and colleagues (2013) measured component "C" of the pupil ellipse, which was calculated as $(1 - PDR)sin[2(\theta - \frac{\pi}{2})]$, where θ is the tilt of the entrance pupil ellipse. Their observed C values are plotted in black. The current model (dashed red line) replicates the Mathur empirical result well (RMSE = 3e-3).

be appreciated in the rendered eye depictions (Fig 3b), with the top of the pupil tilted towards the nasal field when the eye is viewed from the temporal field, and vice-a-versa. This tilt is almost entirely the result of modeling the vertical displacement of the visual axis from the optical axis; there is a small additional effect of the tilt of the dilated pupil aperture ellipse.

Error in ellipse fitting to entrance pupil boundary

Finally, I examined how well the entrance pupil is described by an ellipse as a function of viewing angle by calculating the root mean squared distance of the entrance pupil border points from the fitted ellipse, expressed in millimeters (Figure 9). Overall, the ellipse fit error is small relative to the 6 mm diameter of the entrance pupil, although this error grows systematically as a function of viewing angle.

Discussion

I find that an exact model eye is able to reproduce empirical measurements of the shape of the entrance pupil with good accuracy. More generally, the current study provides a forward model of the appearance of the pupil as observed by a camera at an arbitrary position.

Similar to the current study, Fedtke and colleagues (7) had the goal of using a ray-traced model eye to examine the properties of the entrance pupil as compared to empirical measures. The current study builds upon this prior work in a few respects. First, the anatomical accuracy of the anterior chamber of the model eye is advanced, incorporating an elliptical pupil aperture and a tri-axial cornea. Second, the misalignment of the visual and optical axes is modeled. These refinements both improve the match to empirical observations (6) and support the generalization of the model to arbitrary pupil sizes and to viewing angles apart from the horizontal plane.

The model is easily extended to account for rotation of the eye. There is an extensive literature in which anatomically-inspired models of the eye are used to inform gaze and pupil tracking systems (e.g., 3; 34). These applications have a particular focus upon determining the location of the first Purkinje image and the center of the entrance pupil, as these may be used to deduce gaze angle. While not studied here, these values could be derived readily from the current model.

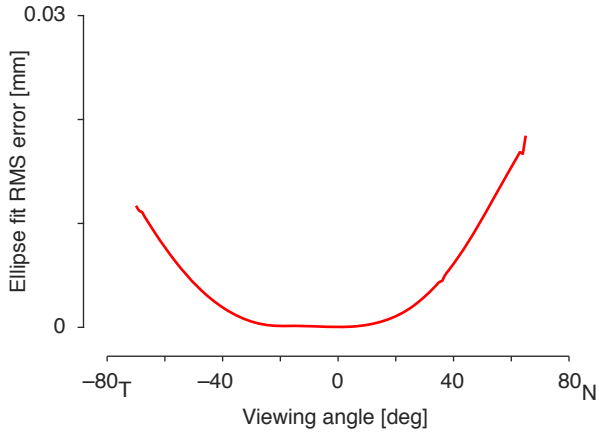

Figure 9. Ellipse fit error. The set of points that define the pupil boundary in the image are not exactly elliptical due to the refractive effects of the cornea. The root mean squared distance of the pupil boundary points from the best fitting ellipse as a function of viewing angle is shown. The fitting error is expressed in mm.

A relevant feature of the current model is that it is implemented in custom made, open-source MATLAB code, as opposed to within general optical bench software (e.g., Zemax). The ray-tracing operations of the model are conducted using compiled functions. As a result, the routines execute quickly and can form the basis of an "inverse model" that searches across values of eye rotation and pupil radius to best fit an observed eye tracking image.

The biometric parameters that define the model were set almost entirely by reference to prior empirical measurements of the central tendency of studied populations. In an effort to best fit the pupil diameter ratio function of Mathur and colleagues (6), however, two model parameters were tuned "by hand": the maximum, dilated entrance pupil ellipticity was held to a value slightly smaller than previously reported (12); and the value for vertical α was set to 3.0° in the emmetropic eye. Because these parameter values are biologically plausible and within the range of prior empirical measurements, I am optimistic that the model will generalize well to novel observations of entrance pupil appearance. Further, the implemention of the model readily accomodates custom biometric measurements of any particular eye to be modeled.

References

1. Bradly, A. & Thibos, L. N. Modeling off-axis vision i: the optical effects of decentering visual targets or the eye's entrance pupil. In *Vision models for target detection and recognition: In memory of Arthur Menendez*, 313–337 (World Scientific, 1995).

2. Uozato, H. & Guyton, D. L. Centering corneal surgical procedures. *Am. journal ophthalmology* **103**, 264–275 (1987).

3. Barsingerhorn, A., Boonstra, F. & Goossens, H. Optics of the human cornea influence the accuracy of stereo eye-tracking methods: a simulation study. *Biomed. optics express* **8**, 712–725 (2017).

4. Spring, K. & Stiles, W. Apparent shape and size of the pupil viewed obliquely. *The Br. journal ophthalmology* **32**, 347 (1948).

5. Jay, B. The effective pupillary area at varying perimetric angles. *Vis. Res.* **1**, 418–424 (1962).

6. Mathur, A., Gehrmann, J. & Atchison, D. A. Pupil shape as viewed along the horizontal visual field. *J. vision* **13**, 3–3 (2013).

7. Fedtke, C., Manns, F. & Ho, A. The entrance pupil of the human eye: a three-dimensional model as a function of viewing angle. *Opt. express* **18**, 22364–22376 (2010).

8. Navarro, R., Santamaria, J. & Bescós, J. Accommodation-dependent model of the human eye with aspherics. *JOSA A* **2**, 1273–1280 (1985).

9. Navarro, R., González, L. & Hernández, J. L. Optics of the average normal cornea from general and canonical representations of its surface topography. *JOSA A* **23**, 219–232 (2006).

10. Atchison, D. A. Optical models for human myopic eyes. *Vis. research* **46**, 2236–2250 (2006).

11. Drexler, W. *et al.* Submicrometer precision biometry of the anterior segment of the human eye. *Investig. Ophthalmol. & Vis. Sci.* **38**, 1304–1313 (1997).

12. Wyatt, H. J. The form of the human pupil. *Vis. Res.* **35**, 2021–2036 (1995).

13. Caroline, P. & Andre, M. The effect of corneal diameter on soft lens fitting, part 2. *Contact Lens Spectr.* **17**, 56–56 (2002).

14. Brückner, B. HVID & SimK study. Tech. Rep., Appenzeller Kontaktlinsen AG (n.d.).

15. Navarro, R. Adaptive model of the aging emmetropic eye and its changes with accommodation. *J. vision* **14**, 21–21 (2014).

16. Jones, C. E., Atchison, D. A., Meder, R. & Pope, J. M. Refractive index distribution and optical properties of the isolated human lens measured using magnetic resonance imaging (mri). *Vis. research* **45**, 2352–2366 (2005).

17. Liou, H.-L. & Brennan, N. A. Anatomically accurate, finite model eye for optical modeling. *JOSA A* **14**, 1684–1695 (1997).

18. Atchison, D. A., Smith, G. & Smith, G. Optics of the human eye. (2000).

19. Tabernero, J., Benito, A., Alcón, E. & Artal, P. Mechanism of compensation of aberrations in the human eye. *JOSA A* **24**, 3274–3283 (2007).

20. Gharaee, H. *et al.* Angle kappa measurements: normal values in healthy Iranian population obtained with the Orbscan II. *Iran. Red Crescent Med. J.* **17** (2015).

21. Tscherning, M. H. E. *Physiologic Optics: Dioptrics of the Eye, Functions of the Retina Ocular Movements and Binocular Vision* (Keystone Publishing Company, 1920).

22. Qi, H., Jiang, J.-J., Jiang, Y.-M., Wang, L.-Q. & Huang, Y.-F. Kappa angles in different positions in patients with myopia during lasik. *Int. journal ophthalmology* **9**, 585 (2016).

23. Bouguet, J.-Y. Matlab camera calibration toolbox (2000).

24. Zhang, Z. A flexible new technique for camera calibration. *IEEE Transactions on pattern analysis machine intelligence* **22**, 1330–1334 (2000).

25. Heikkila, J. & Silven, O. A four-step camera calibration procedure with implicit image correction. In *Computer Vision and Pattern Recognition, 1997. Proceedings., 1997 IEEE Computer Society Conference on*, 1106–1112 (IEEE, 1997).

26. Fitzgibbon, A., Pilu, M. & Fisher, R. B. Direct least square fitting of ellipses. *IEEE Transactions on pattern analysis machine intelligence* **21**, 476–480 (1999).

27. Childs, A. *et al.* Fabricating customized hydrogel contact lens. *Sci. reports* **6**, 34905 (2016).

28. Nikolov, I. D. & Ivanov, C. D. Optical plastic refractive index measurements for nir region. In *18th Congress of the International Commission for Optics*, vol. 3749, 554–556 (International Society for Optics and Photonics, 1999).

29. Nikolov, I. D. & Ivanov, C. D. Optical plastic refractive measurements in the visible and the near-infrared regions. *Appl. Opt.* **39**, 2067–2070 (2000).

30. Sardar, D. K., Swanland, G.-Y., Yow, R. M., Thomas, R. J. & Tsin, A. T. Optical properties of ocular tissues in the near infrared region. *Lasers medical science* **22**, 46–52 (2007).

31. Traynor, N. B. *et al.* Cr-39 (padc) reflection and transmission of light in the ultraviolet–near-infrared (uv–nir) range. *Appl. spectroscopy* 0003702817745071 (2017).

32. Langenbucher, A., Viestenz, A., Viestenz, A., Brünner, H. & Seitz, B. Ray tracing through a schematic eye containing second-order (quadric) surfaces using 4×4 matrix notation. *Ophthalmic Physiol. Opt.* **26**, 180–188 (2006).

33. Kyei, S., Nketsiah, A. A., Asiedu, K., Awuah, A. & Owusu-Ansah, A. Onset and duration of cycloplegic action of 1% cyclopentolate–1% tropicamide combination. *Afr. health sciences* **17**, 923–932 (2017).

34. Böhme, M., Dorr, M., Graw, M., Martinetz, T. & Barth, E. A software framework for simulating eye trackers. In *Proceedings of the 2008 symposium on Eye tracking research & applications*, 251–258 (ACM, 2008).

Acknowledgements

Grant support provided by the NIH (U01EY025864, R01EY024681, P30EY001583).

Author contributions statement

G.K.A. performed the study.

Additional information

Competing interests The author declares no competing interests. **Data availability** The code used to perform these simulations and produce the figures may be found here: (https://github.com/gkaguirrelab/Aguirre_2018_NatSciReports)